




Dynamic effect of constant inertial acceleration on vibration isolation system with high-order stiffness and Bouc–Wen hysteresis

Mu-Qing Niu · Li-Qun Chen 

Received: 17 March 2020 / Accepted: 13 January 2021 / Published online: 3 February 2021
© The Author(s), under exclusive licence to Springer Nature B.V. part of Springer Nature 2021

Abstract Nonlinear vibration isolation provides with an effective way for vibration reduction with broad band and high efficiency. This investigation focuses on the dynamic effects of a constant inertial acceleration on a nonlinear vibration isolation system with high-order stiffness and Bouc–Wen hysteresis. A wire rope-based isolator subject to the inertial acceleration is analyzed to illustrate the uncertainty of the static equilibrium state and the diverse dynamic effects of the acceleration. The frequency responses are obtained through a semianalytical method based on the harmonic balance method. A recursive method is proposed to deal with the polynomial function derived from the nonlinear stiffness. An alternating frequency/time domain technique is adopted to treat the implicit function of the Bouc–Wen hysteresis. The calculation results are verified by a numerical simulation with the Runge–Kutta method. The analysis and the simulations reveal that the inertial acceleration leads to different static equilibrium states according to the paths to the equilibriums. The inertial acceleration, respectively, affects the static equilibrium displacement and the residual hysteretic force, and they change the dynamic responses differently. The acceleration effect on the static equilibrium displacement leads to additional coupling stiffness making the system

harder/softer with positive/negative high-order stiffness. Furthermore, the acceleration has a significant effect on the dynamic equilibrium location, and the equilibrium reaches the minimum around the resonance and increases gradually at higher frequencies. The acceleration effect on the residual hysteretic force changes the amplitude–frequency responses indirectly through additional coupling stiffness. A positive residual hysteretic force leads to a positive overall deviation of the dynamic equilibrium location regardless of the positive or negative high-order stiffness.

Keywords Nonlinear vibration isolation · Inertial acceleration · Bouc–Wen hysteresis · Harmonic balance method

1 Introduction

Vibration isolation systems are extensively used in space engineering to provide with a stable working condition for the payloads. At initial conditions, the isolators are statically balanced under a preset inertial acceleration, such as the Earth's gravity or the centrifugal acceleration of the expected orbit. However, at working conditions, the inertial acceleration exerted on the isolator may be very different from the preset one in some cases, such as launching, running

M.-Q. Niu · L.-Q. Chen (✉)
School of Science, Harbin Institute of Technology,
Shenzhen 518055, China
e-mail: chenliqun@hit.edu.cn

on an elliptical orbit, or being attracted by a star. The additional acceleration applied on the isolator can be regarded as a time-dependent fluctuation about a temporal-average value. The acceleration fluctuation can be modeled as a periodic or even a stochastic excitation, while the average is a time-independent constant for a period of time. In some circumstances, the constant inertial acceleration is too large to be neglected. Therefore, the understanding of its additional dynamic effects is significant to design vibration isolators. For linear systems, a constant inertial acceleration can be balanced by the static deflection force. Therefore, its dynamic effect can be ignored if the vibration is measured from the new static equilibrium location. However, the practice does not work for nonlinear systems. Chen et al. [1] revealed the dynamic effects of the gravity on a nonlinear energy sink moving vertically. For a nonlinear system with cubic stiffness, the gravity leads to additional linear and quadratic terms in the dynamic equations. Hence the exact prediction of the response should account for the gravitational acceleration. The nonlinear system treated by Chen et al. [1] is with a single-valued restoring force, and thus the static equilibrium location and the dynamic response can be completely determined by the inertial acceleration. However, the situation is much more complicated for a nonlinear system with a multi-valued restoring force, such as a hysteretic system. More kinds of coupling terms are induced and the static equilibrium state is not unique under a certain inertial acceleration. With the diversity of the coupling terms and the uncertainty of the static equilibrium state, dynamic effects of the inertial acceleration remain unclear for such systems. To address the lack of investigations on this aspect, the work explores the dynamic effect of a constant inertial acceleration on a vibration isolator with high-order stiffness and hysteretic damping.

The promising methods to analyze dynamic systems with strong nonlinearities are divided into analytical methods, semianalytical methods and numerical methods. Typical analytical methods include the harmonic balance method (HBM) [2], the averaging method [3] and the perturbation method [4]. Semianalytical methods are based on analytical methods with numerical techniques dealing with the nonlinear terms. A typical example of numerical method is the Poincaré map method [5]. Systems with the nonlinear terms expressed by single-valued

explicit functions are often solved by analytical/semianalytical methods. Typical examples include the systems with high-order stiffness [6], piecewise stiffness [7], and nonlinear viscous damping expressed by a single-valued function of the velocity [8] or both the velocity and the displacement [9]. Lu et al. [10] adopted a HBM to study the root-mean-square transmissibility of an isolator with cubic stiffness. Wang et al. [7] approximately solved a nonlinear system with piecewise stiffness by an averaging method. Yang et al. [11] calculated the power flow and the force transmission of an isolator with both cubic stiffness and cubic damping by an averaging method. Huang et al. [12] investigated the isolation performance of a velocity-displacement-dependent nonlinear viscous damping by an averaging perturbation method. The analysis is much more complicated for the systems with the nonlinear terms expressed by multi-valued functions, such as most hysteretic systems. In some cases, the continuous and smooth hysteretic restoring forces can be fitted into elliptic functions [13] or made equivalent to nonlinear viscous damping forces [14] with considerable accuracy. Otherwise, numerical techniques are necessary for the analysis. Bilinear hysteresis can be expressed by piecewise functions. Xiong et al. [15] and Wu et al. [16] analyzed nonlinear systems with cubic stiffness and bilinear hysteresis by the increment harmonic balance method, and the calculation problem resulting from the piecewise function is solved with a Galerkin process. Most hysteresis can be characterized by phenomenological models, such as Masing model [17] and Bouc–Wen model [18], expressed by implicit functions. Wong et al. [19] treated a Bouc–Wen hysteretic system with a semianalytical method based on the HBM and the Levenberg–Marquardt algorithm. Lacarbonara and Vestroni [20] numerically solved both the Masing-type and the Bouc–Wen-type hysteretic systems, and sought the periodic orbits with the Poincaré map. However, the research on the semianalytical analysis of the systems with both high-order stiffness and Bouc–Wen hysteresis is rather limited. It is challenging because both a polynomial function and an implicit function are included in the dynamic equations. Although it is feasible to adopt numerical techniques, such as alternating frequency/time domain technique (AFT) [21, 22], on each kind of nonlinear functions, the computing cost increases remarkably with the times of using AFT. It is expected to reduce the need of

AFT by analytical deduction. Besides, in most investigations, restoring forces are symmetric about the static equilibrium locations, and there is no zero-order harmonic component in the periodic responses. However, the zero-order component is frequency-dependent under a unidirectional inertial acceleration. It is denoted as the dynamic equilibrium displacement and is one of the focuses in the following analysis.

Wire rope-based structure is a typical design providing with hysteretic damping due to inner friction. It has been adopted in Stockbridge dampers [23] and helical isolators [24]. Carpineto et al. [25] proposed a tuned mass damper with the wire rope fixed at one end and constrained by a slide bearing at the other end. In this way, stiffness nonlinearity is produced in addition to the hysteretic damping. Carboni et al. [26, 27] improved the structure by replacing the slide bearing with an elastic axial constraint in order to adjust the stiffness nonlinearity. The structure has been used for vibration-absorbing experiments [28]. The wire rope-based structure with axial constraint is adopted in the vibration isolator for a case study in the present work.

This work explores the dynamic effects of a constant inertial acceleration on a vibration isolation system with both stiffness and damping nonlinearities. The high-order stiffness is expressed by a polynomial function, and the Bouc–Wen hysteretic damping is characterized by a multi-valued implicit function. The investigation focuses on the additional coupling terms and the uncertainty of the static equilibrium state due to the inertial acceleration. To solve the dynamic model with diverse nonlinearities, a semianalytical method based on HBM and AFT is adopted and modified by an analytical deduction through a recursive method. A wire rope-based isolator is treated as a case study. The results reveal the dynamic effects of the inertial acceleration via determining the frequency responses of the harmonic components, especially the zero-order component.

The following manuscript is organized as follows. In Sect. 2, the vibration isolation model under a constant inertial acceleration is described. In Sect. 3, a semianalytical method is proposed to seek the frequency responses. In Sect. 4, a wire rope-based nonlinear isolator is introduced and modeled. In Sect. 5, numerical simulations are performed to demonstrate the static equilibrium states, frequency responses and parameter effects of the system. Section 6 yields the conclusions.

2 Model description

Consider a nonlinear vibration isolation system with high-order stiffness and hysteretic damping. The nonlinear stiffness and damping are expressed by a polynomial function and a first-order Bouc–Wen model [18], respectively. The payload displacement, the base displacement and their relative displacement are denoted as X_{p0} , X_b and X_0 , respectively. When a constant inertial acceleration is applied on the payload, the dynamic equations of the system are

$$MX''_{p0} + \sum_{i=1}^n K_i X_0^i + Z = MA_{in} \tag{1}$$

$$Z' = \{K_d - [G + B \operatorname{sgn}(\dot{X}_0 Z)]|Z|\} X'_0 \tag{2}$$

where M , K_i , Z and A_{in} denote the payload mass, the coefficient of i th-order stiffness, the hysteretic force and the inertial acceleration, respectively. K_d , G and B are Bouc–Wen model parameters. At static equilibrium state, there is

$$\sum_{i=1}^n K_i X_s^i + Z_s = MA_{in} \tag{3}$$

where X_s and Z_s are the relative displacement and the hysteretic force at the static equilibrium state. The base excitation is assumed to be harmonic with the amplitude A_e and the frequency ω_e , i.e. $X_b = A_e \cos(\omega_e T)$. Assuming $X = X_0 - X_s$ and subtracting Eq. (3) from Eq. (1) leads to

$$\begin{aligned} MX'' + \sum_{i=1}^n \left[X^i \sum_{j=i}^n \frac{j! K_j X_s^{j-i}}{i!(j-i)!} \right] + Z - Z_s \\ = MA_e \omega_e^2 \cos(\omega_e T) \end{aligned} \tag{4}$$

Introduction of dimensionless parameters transform Eqs. (2), (3) and (4) into

$$\begin{aligned} \eta^2 \ddot{x} + \delta x + \sum_{i=2}^n k_i x^i + x \sum_{i=2}^n i k_i x_s^{i-1} \\ + \sum_{i=2}^{n-1} \left[x^i \sum_{j=i+1}^n \frac{j! k_j x_s^{j-i}}{i!(j-i)!} \right] + (1 - \delta)(z - z_s) \\ = \eta^2 a_e \cos t \end{aligned} \tag{5}$$

$$\dot{z} = \{1 - [\gamma + \beta \operatorname{sgn}(\dot{x}z)]|z|\} \dot{x} \tag{6}$$

$$\delta x_s + \sum_{i=2}^n k_i x_s^i + (1 - \delta) z_s = a_{in} \tag{7}$$

where

$$\begin{aligned} \omega_c &= \sqrt{\frac{K_1 + K_d}{M}}, \quad t = \omega_c T, \quad \delta = \frac{K_1}{K_1 + K_d}, \\ k_i &= \frac{K_i X_c^{i-1}}{K_1 + K_d}, \quad x = \frac{X}{X_c}, \quad x_s = \frac{X_s}{X_c}, \\ z &= \frac{Z}{K_d X_c}, \quad z_s = \frac{Z_s}{K_d X_c}, \quad a_{in} = \frac{A_{in}}{\omega_c^2 X_c}, \quad \gamma = GX_c, \\ \beta &= BX_c, \quad a_e = \frac{A_e}{X_c}, \quad \eta = \frac{\omega_e}{\omega_c} \end{aligned} \tag{8}$$

where ω_c and X_c are the characteristic frequency and the characteristic displacement, respectively.

Equation (7) shows that the static equilibrium state depends on both the static equilibrium displacement x_s and the residual hysteretic force z_s . An inertial acceleration may lead to diverse static equilibrium states. Furthermore, the inertial acceleration has separate dynamic effects on x_s and z_s as shown in Eq. (5). Due to the acceleration effect on x_s , there are additional linear and high-order coupling stiffness presented as the 4th and 5th terms in Eq. (5), respectively. The acceleration effect on z_s affects the hysteretic force.

3 Methodology

To solve Eqs. (5) and (6), a semianalytical method based on HBM is adopted. Assume the following Fourier expansions

$$x = a_0 + \sum_{i=1}^m [a_i \cos(it) + b_i \sin(it)] \tag{9}$$

$$x^j = p_0^{(j)} + \sum_{i=1}^m [p_i^{(j)} \cos(it) + q_i^{(j)} \sin(it)] \tag{10}$$

$$z = c_0 + \sum_{i=1}^m [c_i \cos(it) + d_i \sin(it)] \tag{11}$$

where $m \geq n$, and $j = 1, 2, \dots, n$. Obviously, there are $p_0^{(1)} = a_0$, $p_i^{(1)} = a_i$ and $q_i^{(1)} = b_i$. For $j > 1$, the expressions of $p_0^{(j)}$, $p_i^{(j)}$ and $q_i^{(j)}$ are calculated based on a recursive method:

$$p_0^{(j)} = \frac{1}{2} \sum_{l=1}^m (p_l^{(j-1)} a_l + q_l^{(j-1)} b_l) + p_0^{(j-1)} a_0 \tag{12}$$

$$\begin{aligned} p_i^{(j)} &= \frac{1}{2} \left[\sum_{l=0}^{m-i} p_l^{(j-1)} a_{l+i} + \sum_{l=i}^m p_l^{(j-1)} a_{l-i} \right. \\ &+ \sum_{l=0}^i p_l^{(j-1)} a_{i-l} + \sum_{l=1}^{m-i} q_l^{(j-1)} b_{l+i} + \sum_{l=i+1}^m q_l^{(j-1)} b_{l-i} \\ &\left. - \sum_{l=1}^{i-1} q_l^{(j-1)} b_{i-l} \right] \end{aligned} \tag{13}$$

$$\begin{aligned} q_i^{(j)} &= \frac{1}{2} \left[\sum_{l=0}^{m-i} p_l^{(j-1)} b_{l+i} + \sum_{l=i}^m q_l^{(j-1)} a_{l-i} \right. \\ &- \sum_{l=1}^{m-i} q_l^{(j-1)} a_{l+i} - \sum_{l=i+1}^m p_l^{(j-1)} b_{l-i} + \sum_{l=0}^{i-1} p_l^{(j-1)} b_{i-l} \\ &\left. + \sum_{l=1}^i q_l^{(j-1)} a_{i-l} \right] \end{aligned} \tag{14}$$

Denote $\mathbf{A} = [a_0, a_1, \dots, a_m, b_1, \dots, b_m]^T$ and $\mathbf{C} = [c_0, c_1, \dots, c_m, d_1, \dots, d_m]^T$. Substituting Eqs. (9), (10) and (11) into Eq. (5) and taking harmonic balance process lead to

$$\begin{aligned} c_0 &= -\frac{1}{1 - \delta} \left\{ \delta a_0 + \sum_{i=2}^n k_i p_0^{(i)} + a_0 \sum_{i=2}^n i k_i x_s^{i-1} \right. \\ &\left. + \sum_{i=2}^{n-1} \left[p_0^{(i)} \sum_{j=i+1}^n \frac{j! k_j x_s^{j-i}}{i!(j-i)!} \right] \right\} + z_s \end{aligned} \tag{15}$$

$$\begin{aligned} c_l &= \frac{1}{1 - \delta} \left\{ \varphi(l) \eta^2 a_e + l^2 \eta^2 - \delta a_l - \sum_{i=2}^n k_i p_l^{(i)} \right. \\ &\left. - a_l \sum_{i=2}^n i k_i x_s^{i-1} - \sum_{i=2}^{n-1} \left[p_l^{(i)} \sum_{j=i+1}^n \frac{j! k_j x_s^{j-i}}{i!(j-i)!} \right] \right\} \end{aligned} \tag{16}$$

$$d_l = \frac{1}{1 - \delta} \left\{ l^2 \eta^2 - \delta b_l - \sum_{i=2}^n k_i q_l^{(i)} - b_l \sum_{i=2}^n i k_i x_s^{i-1} - \sum_{i=2}^{n-1} \left[q_l^{(i)} \sum_{j=i+1}^n \frac{j! k_j x_s^{j-i}}{i!(j-i)!} \right] \right\} \quad (17)$$

where $\varphi(l) = \begin{cases} 1, & l = 1 \\ 0, & l \neq 1 \end{cases}$. Thus, the Fourier expansion of z is expressed in explicit functions through an analytical deduction based on Eq. (5). The residual r is given through Eq. (6):

$$r = \dot{z} - \{1 - [\gamma + \beta \text{sgn}(\dot{x}z)]|z|\} \dot{x} \quad (18)$$

and the Fourier expansion of r is expressed as

$$r = u_0 + \sum_{i=1}^m [u_i \cos(it) + v_i \sin(it)] \quad (19)$$

Denote $\mathbf{U} = [u_0, u_1, \dots, u_m, v_1, \dots, v_m]^T$ and it is calculated through AFT. Define a discrete time sequence from $t = 0$ to $t = 2\pi$. With the values of \mathbf{A} determined, $\dot{x}(t)$, $z(t)$ and $\dot{z}(t)$ can be calculated as discrete sequences. Then $r(t)$ is acquired through Eq. (18). \mathbf{U} is obtained by applying fast Fourier transform on $r(t)$. Hence \mathbf{U} is a function of \mathbf{A} . When \mathbf{A} is the exact solution of the dynamic equations, there is $\mathbf{U} = \mathbf{0}$. Therefore, solving \mathbf{A} is equivalent to the least-mean-square problem of searching \mathbf{A} to achieve the minimum value of $\|\mathbf{U}\|_2$. A Levenberg–Marquardt algorithm [19] is adopted to seek the least-mean-square solution with the iteration formula of

$$\mathbf{A}^{(k+1)} = \mathbf{A}^{(k)} - \left\{ \mathbf{J}_{[\mathbf{A}^{(k)}]}^T \mathbf{J}_{[\mathbf{A}^{(k)}]} + \varphi^{(k)} \mathbf{I} \right\}^{-1} \mathbf{J}_{[\mathbf{A}^{(k)}]}^T \mathbf{U}_{[\mathbf{A}^{(k)}]} \quad (20)$$

where the superscript denotes the number of iterations, and φ is the Levenberg–Marquardt parameter. \mathbf{I} is the identity matrix. $\mathbf{J} = [\partial \mathbf{U} / \partial a_0; \partial \mathbf{U} / \partial a_1; \dots; \partial \mathbf{U} / \partial a_m; \partial \mathbf{U} / \partial b_1; \dots; \partial \mathbf{U} / \partial b_m]$ is the Jacobi matrix of \mathbf{U} and is calculated through analytical deduction and AFT. Firstly, the partial derivatives of $p_0^{(j)}$, $p_i^{(j)}$ and $q_i^{(j)}$ are calculated as

$$\frac{\partial p_0^{(j)}}{\partial a_0} = j p_0^{(j-1)} \quad \frac{\partial p_0^{(j)}}{\partial a_i} = \frac{j}{2} p_i^{(j-1)} \quad \frac{\partial p_0^{(j)}}{\partial b_i} = \frac{j}{2} q_i^{(j-1)} \quad (21)$$

$$\begin{cases} \frac{\partial p_i^{(j)}}{\partial a_0} = j p_i^{(j-1)} \\ \frac{\partial p_i^{(j)}}{\partial a_l} = \frac{j}{2} [\psi(l-i) p_{l-i}^{(j-1)} + \psi(l+i) p_{l+i}^{(j-1)} + \psi(i-l) p_{i-l}^{(j-1)}] \\ \frac{\partial p_i^{(j)}}{\partial b_l} = \frac{j}{2} [\psi^*(l-i) q_{l-i}^{(j-1)} + \psi^*(l+i) q_{l+i}^{(j-1)} - \psi^*(i-l) q_{i-l}^{(j-1)}] \end{cases} \quad (22)$$

$$\begin{cases} \frac{\partial q_i^{(j)}}{\partial a_0} = j q_i^{(j-1)} \\ \frac{\partial q_i^{(j)}}{\partial a_l} = \frac{j}{2} [-\psi^*(l-i) q_{l-i}^{(j-1)} + \psi^*(l+i) q_{l+i}^{(j-1)} + \psi^*(i-l) q_{i-l}^{(j-1)}] \\ \frac{\partial q_i^{(j)}}{\partial b_l} = \frac{j}{2} [\psi(l-i) p_{l-i}^{(j-1)} - \psi(l+i) p_{l+i}^{(j-1)} + \psi(i-l) p_{i-l}^{(j-1)}] \end{cases} \quad (23)$$

where $\psi(x) = \begin{cases} 1, & 0 \leq x \leq m \\ 0, & \text{else} \end{cases}$ and $\psi^*(x) = \begin{cases} 1, & 1 \leq x \leq m \\ 0, & \text{else} \end{cases}$.

Taking the calculation of $\partial \mathbf{U} / \partial a_l$ as an example, denote $\mathbf{T} = [\partial p_0^{(j)} / \partial a_l; \partial p_1^{(j)} / \partial a_l; \dots; \partial p_m^{(j)} / \partial a_l; \partial q_1^{(j)} / \partial a_l; \dots; \partial q_m^{(j)} / \partial a_l]^T$. According to Eq. (5), there is

$$\mathbf{T}_z = \frac{1}{1 - \delta} \left\{ \sum_{i=2}^n \left[k_i + \sum_{j=i+1}^n \frac{j! k_j x_s^{j-i}}{i!(j-i)!} \right] \mathbf{T} - \left(\delta + \sum_{i=2}^n i k_i x_s^{i-1} \right) \mathbf{I}_z \right\} \quad (24)$$

where \mathbf{T}_z is a transformation vector. \mathbf{I}_z is a vector with the same dimension with \mathbf{T}_z , and all the elements are 1. Then the following partial derivatives can be calculated as

$$\frac{\partial z}{\partial a_l} = [1 \cos(t) \dots \cos(mt) \sin(t) \dots \sin(mt)] \mathbf{T}_z \quad (25)$$

$$\frac{\partial \dot{z}}{\partial a_l} = [0 - \sin(t) \dots - m \sin(mt) \cos(t) \dots m \cos(mt)] \mathbf{T}_z \quad (26)$$

According to Eq. (18), there is

$$\begin{aligned} \frac{\partial r}{\partial a_l} &= \frac{\partial r}{\partial \dot{x}} \frac{\partial \dot{x}}{\partial a_l} + \frac{\partial r}{\partial z} \frac{\partial z}{\partial a_l} + \frac{\partial r}{\partial \dot{z}} \frac{\partial \dot{z}}{\partial a_l} \\ &= i \{ [\gamma + \beta \text{sgn}(\dot{x}z)] |z| - 1 \} \sin(it) + [\gamma \text{sgn}(z) \\ &\quad + \beta \text{sgn}(\dot{x})] \dot{x} \frac{\partial z}{\partial a_l} + \frac{\partial \dot{z}}{\partial a_l} \end{aligned} \quad (27)$$

Equation (27) is calculated as a discrete sequence in the time domain. Then $\partial \mathbf{U} / \partial a_l$ can be obtained by

applying fast Fourier transform on $\partial r/\partial a_i$. The rest columns of \mathbf{J} can be acquired with similar procedures. The iteration procedure of the Levenberg–Marquardt algorithm can be found in [19].

The swept frequency method is invalid around the turning points, hence a swept amplitude method is supplemented. Choose a harmonic component which changes monotonically and dramatically around the turning point, such as a_1 . The increment parameter η is replaced by a_1 . \mathbf{A}^* is derived by replacing a_1 in \mathbf{A} with η . The Jacobi matrix \mathbf{J}^* is modified by replacing the second column from $\partial r/\partial a_1$ to $\partial r/\partial \eta$, which is

$$\begin{aligned} \frac{\partial r}{\partial \eta} &= \frac{\partial r}{\partial \dot{x}} \frac{\partial \dot{x}}{\partial \eta} + \frac{\partial r}{\partial z} \frac{\partial z}{\partial \eta} + \frac{\partial r}{\partial \dot{z}} \frac{\partial \dot{z}}{\partial \eta} \\ &= [\gamma \text{sgn}(z) + \beta \text{sgn}(\dot{x})] \dot{x} \frac{\partial z}{\partial \eta} + \frac{\partial \dot{z}}{\partial \eta} \end{aligned} \tag{28}$$

where the partial derivatives on the right side are calculated as follows. Denote matrix \mathbf{T}^* as

$$\mathbf{T}^* = \frac{1}{1-\delta} [0 \quad 2\eta(a_1 + a_c) \dots 2\eta m^2 a_m \quad 2\eta b_1 \dots 2\eta m^2 b_m]^T \tag{29}$$

Then

$$\frac{\partial z}{\partial \eta} = [1 \quad \cos(t) \dots \cos(mt) \quad \sin(t) \dots \sin(mt)] \mathbf{T}^* \tag{30}$$

$$\frac{\partial \dot{z}}{\partial \eta} = [0 \quad -\sin(t) \dots -m \sin(mt) \quad \cos(t) \dots m \cos(mt)] \mathbf{T}^* \tag{31}$$

The calculation procedure is similar with the swept frequency method. Finally, the frequency responses are obtained by the combined results of the swept frequency process and the swept amplitude process.

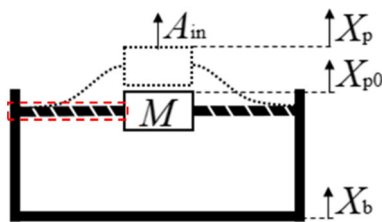


Fig. 1 Wire rope-based vibration isolation system

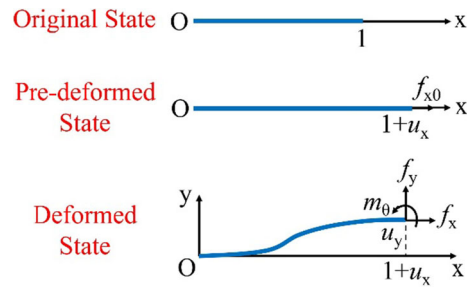


Fig. 2 Dimensionless cantilever beam model

4 Wire rope-based vibration isolation system

A wire rope-based vibration isolation system is shown in Fig. 1. The payload is connected to the base with two wire ropes symmetrically. Solid lines show the horizontal pre-deformed state. Dotted lines show the static equilibrium state with a constant inertial acceleration denoted as A_{in} . The payload mass is denoted as M . The base displacement is denoted as X_b . The payload displacements measured from the pre-deformed state and the static equilibrium state are denoted as X_{p0} and X_p , respectively. When a relative movement between the payload and the base occurs, the wire ropes deform on bending and axial directions, inducing a nonlinear elastic restoring force on the payload. Furthermore, a hysteretic restoring force occurs due to the frictional contact among the wires.

To illustrate the characteristics of the nonlinear elastic restoring force, one of the wire ropes is picked out, as shown in the red dashed box in Fig. 1. The wire rope is assumed to be a constant-section cantilever beam without inner friction. The original length, the Young’s modulus, the section area and the inertial moment of the beam are denoted as L , E , A and I , respectively. A dimensionless model is established, as shown in Fig. 2. The characteristic length, the force and the moment for dimensionless transform are L , EI/L^2 and EIL , respectively. Thus, the original dimensionless length of the beam is 1. When the wire rope is horizontally mounted onto the isolator, it is pre-deformed with an axial force, and the length becomes $1 + u_x$. Because of the symmetric structure shown in Fig. 1, the free end of the beam is only able to move vertically. Therefore, at deformed state, the horizontal displacement is still u_x , and the rotation angle at the free end is constrained to be 0. The vertical displacement is denoted as u_y . The forces and the moment

applied on the free end are denoted as f_x, f_y and $m\theta$, respectively.

According to the beam constraint model [29], at deformed state, there is

$$f_y = \begin{cases} \frac{r^3 \sinh r}{2 + r \sinh r - 2 \cosh r} u_y & f_x \geq 0, r = \sqrt{f_x} \\ \frac{r^3 \sin r}{2 - r \sin r - 2 \cos r} u_y & f_x < 0, r = \sqrt{-f_x} \end{cases} \quad (32)$$

Taylor expansions of Eq. for tension ($f_x \geq 0$) and compression ($f_x < 0$) states are the same, which is

$$f_y = \left(12 + \frac{6}{5}f_x - \frac{1}{700}f_x^2 + \frac{1}{63000}f_x^3 - \dots \right) u_y \quad (33)$$

The axial deformation can be calculated according to a beam arc-length conservation relation [29]:

$$1 + \frac{f_x}{EA} = \int_0^{1+u_x} \sqrt{1 + [y'(x)]^2} dx \quad (34)$$

where $y(x)$ is the shear deformation function of the location x . The relation among u_x, u_y and f_x can be deducted from Eqs. (32) and (34) with different expressions for tension and compression states. Again, their Taylor expansions are the same, which is

$$u_x = \frac{Af_x}{I} - \left(\frac{3}{5} - \frac{1}{700}f_x + \dots \right) u_y^2 \quad (35)$$

Assume that A/I is much larger than $u_y^2/700$, so only constant term is reserved for the coefficient of u_y^2 . According to the pre-deformed state, the horizontal displacement is $u_x = Af_{x0}/I$, and

$$u_x = \frac{Af_x}{I} - \frac{3}{5}u_y^2 = \frac{Af_{x0}}{I} \quad (36)$$

Truncation error of the Taylor expansion in Eq. (33) depends on f_x . We reserve the first three terms. Substituting Eq. (36) into Eq. (33) leads to

$$f_y = \left(12 + \frac{6}{5}f_{x0} - \frac{1}{700}f_{x0}^2 \right) u_y + \left(\frac{18I}{25A} - \frac{3I}{1750A}f_{x0} \right) u_y^3 - \frac{3I}{3500A}u_y^5 \quad (37)$$

It can be seen from Eq. (37) that, if the wire ropes in Fig. 1 are regarded as constant-section beams without inner friction, the vertical restoring force is a function of the vertical displacement with linear term, cubic term and 5th-order term. The coefficient of linear term

can be negative when the pre-force is compression and large enough, and it is the basis for the high-static-low-dynamic stiffness design. For a wire rope, the elastic restoring force expression is similar to Eq. (37) with different coefficients because of the changing section. Hysteretic restoring force due to inner friction can be expressed by a first-order Bouc–Wen model. Therefore, the total dimensionless restoring force f_r of the two wire ropes shown in Fig. 1 can be expressed as

$$f_r = k_1x_0 + k_3x_0^3 + k_5x_0^5 + z \quad (38)$$

where $x_0 = x_{p0} - x_b$ and z is expressed in Eq. (6). Therefore, under a harmonic base excitation, the dimensionless dynamic equation of the isolator without inertial acceleration is expressed as

$$\eta^2\ddot{x} + \delta x + k_3x^3 + k_5x^5 + (1 - \delta)z = \eta^2a_e \cos t \quad (39)$$

Applying the formulation process introduced in Sect. 2, the dimensionless dynamic equation under a constant inertial acceleration can be expressed as

$$\begin{aligned} \eta^2\ddot{x} + (\delta + 3k_3x_s^2 + 5k_5x_s^4)x + (3k_3x_s + 10k_5x_s^3)x^2 \\ + (k_3 + 10k_5x_s^2)x^3 \\ + 5k_5x_sx^4 + k_5x^5 + (1 - \delta)(z - z_s) = \eta^2a_e \cos t \end{aligned} \quad (40)$$

and the static equilibrium state is expressed as

$$\delta x_s + k_3x_s^3 + k_5x_s^5 + (1 - \delta)z_s = a_{in} \quad (41)$$

Equation (39) indicates that, without inertial acceleration, there are only odd-order stiffness terms, and the restoring force is symmetric about the static equilibrium location. With inertial acceleration, as indicated by Eq. (40), coupling stiffness terms derive from higher-order stiffness. Odd-order stiffness terms and the residual hysteretic force occur, leading to an asymmetric restoring force.

The values of δ, k_3, k_5, β and γ depend on the wire rope material, winding type, dimensions and pre-force. Their values in the following numerical simulation are selected from the parameter space identified with a similar wire rope-based device shown in [30].

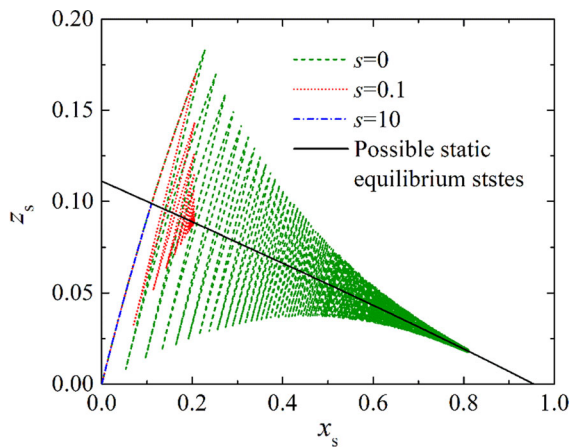


Fig. 3 Possible path for payload reaching static equilibrium

5 Analysis and simulations

5.1 Static equilibrium state analysis

According to Eq. (39), an inertial acceleration may lead to diverse static equilibrium states determined by both x_s and z_s . Due to the historical dependence of the Bouc–Wen hysteresis, the static equilibrium state depends on the paths to the equilibrium, as shown in the following simulation. Assume that the wire ropes are at horizontal state without any residual hysteretic force, and an inertial acceleration is applied instantaneously. The process that the payload gradually reaches static equilibrium can be expressed as the following dynamic equation

$$\ddot{x} + s\dot{x} + \delta x + k_3x^3 + k_5x^5 + (1 - \delta)z = a_{in} \quad (42)$$

where s adjusts the path that payload reaches static equilibrium. When $s = 0$, the payload reaches static equilibrium freely. When s is large enough, the payload reaches static equilibrium in a quasi-static way.

Determine the parameters as $\delta = 0.1$, $k_3 = 5 \times 10^{-3}$, $k_5 = 10^{-4}$, $\beta = \gamma = 1$ and $a_{in} = 0.1$. Equation (42) is solved numerically with a fourth-order Runge–Kutta method. The results for $s = 0, 0.1$ and 10 are shown in Fig. 3. With smaller s , more oscillations occur before the payload reaches static equilibrium. The resulting x_s tends to be larger and z_s tends to be smaller. The solid line shows the possible values for x_s and z_s in static equilibrium states according to Eq. (41).

5.2 Frequency responses

This section investigates the frequency responses of the system under a harmonic displacement excitation from the base. Determine the parameters as $\delta = 0.1$, $k_3 = 5 \times 10^{-3}$, $k_5 = 10^{-4}$, $\beta = \gamma = 1$ and $a_e = 1$. The inertial acceleration has separate effects on x_s and z_s , and they influence the dynamic responses differently. In the following analysis, there are four groups of x_s and z_s values for comparison: (a) $x_s = z_s = 0$; (b) $x_s = 0.71$, $z_s = 0$; (c) $x_s = 0$, $z_s = 0.03$; (d) $x_s = 0.71$, $z_s = 0.03$.

The responses are computed by the semianalytical method proposed in Sect. 3 and $m = 5$. The amplitude of the i th-order harmonics of x is denoted as amp_i and calculated as

$$amp_i = \sqrt{a_i^2 + b_i^2} \quad (43)$$

where $i = 1, 2, \dots, 5$. Calculated results of the first- to fifth-order harmonic amplitudes are shown in Fig. 4a–d. When $x_s = z_s = 0$ (without inertial acceleration), there is no even-order harmonic component. There are super-harmonic resonances at $\eta = 1/3$ and $\eta = 1/5$. When x_s or z_s is nonzero (with inertial acceleration), the even-order harmonics occur due to the asymmetric restoring force. There are additional super-harmonic resonances at $\eta = 1/2$ and $\eta = 1/4$. Amplitude variations of the odd-order harmonics are rather small compared with their amplitudes. Still, the differences can be spotted at $\eta = 1/2$ and $\eta = 1/4$. Take the second-order harmonic amplitude as an example, as shown in Fig. 4e. The amplitude with $(x_s = 0.71, z_s = 0.03)$ approximately equals the summation of the amplitudes with $(x_s = 0.71, z_s = 0)$ and $(x_s = 0, z_s = 0.03)$. It can be concluded that the effects of x_s and z_s on the harmonic amplitudes can be regarded as decoupling.

As shown in Fig. 4f, a_0 illustrates the dynamic equilibrium location change relative to the static equilibrium location. a_0 increases dramatically at low frequency due to the acceleration effect on z_s . It reaches the maximum at $\eta = 0.47$. The dynamic equilibrium location decreases dramatically when η exceeds 0.47, and then increases gradually at higher frequencies. A positive z_s leads to a positive overall deviation of a_0 . With the contrast of Fig. 4a–f, it is obvious that the inertial acceleration has greater

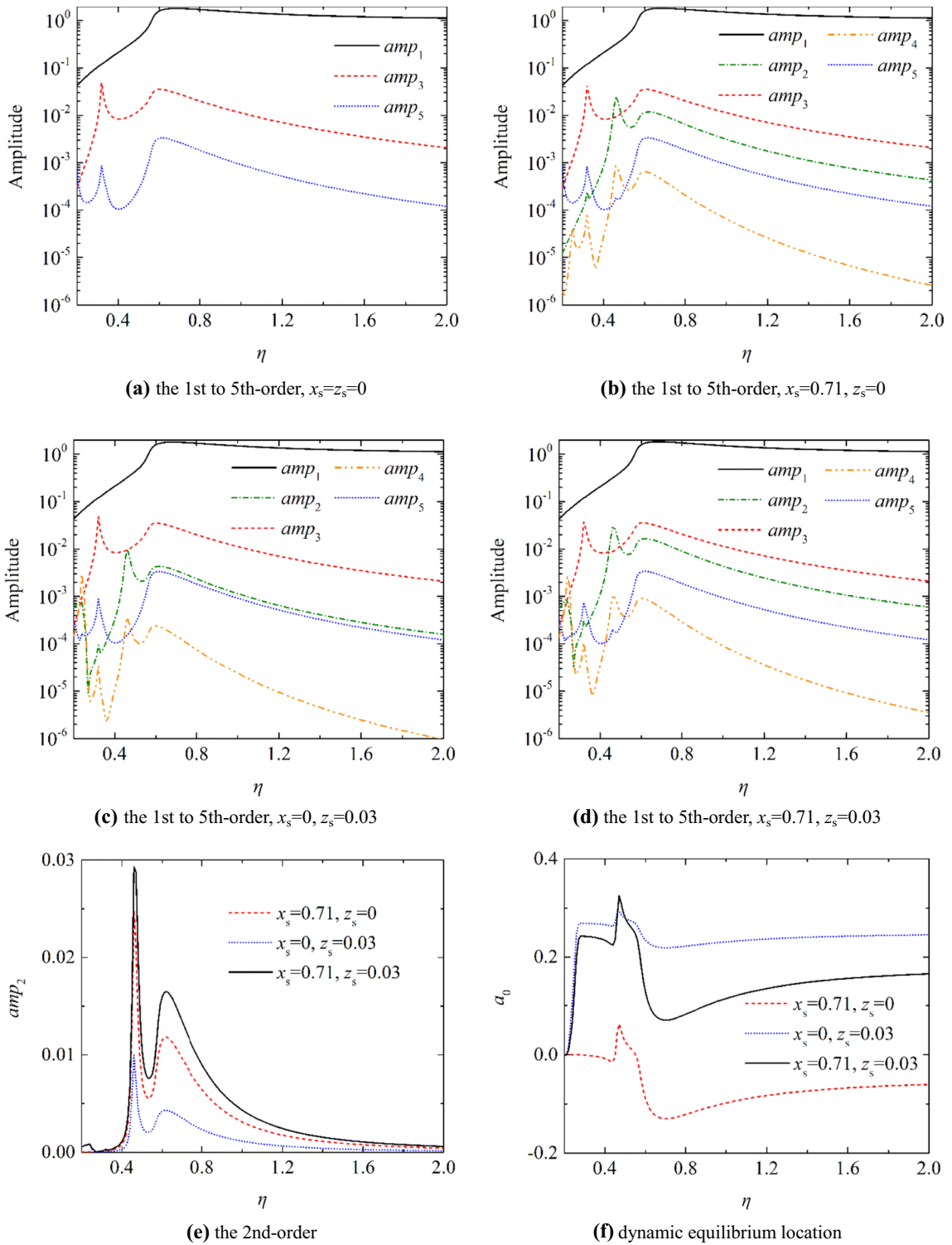


Fig. 4 Amplitudes of different order harmonics of x

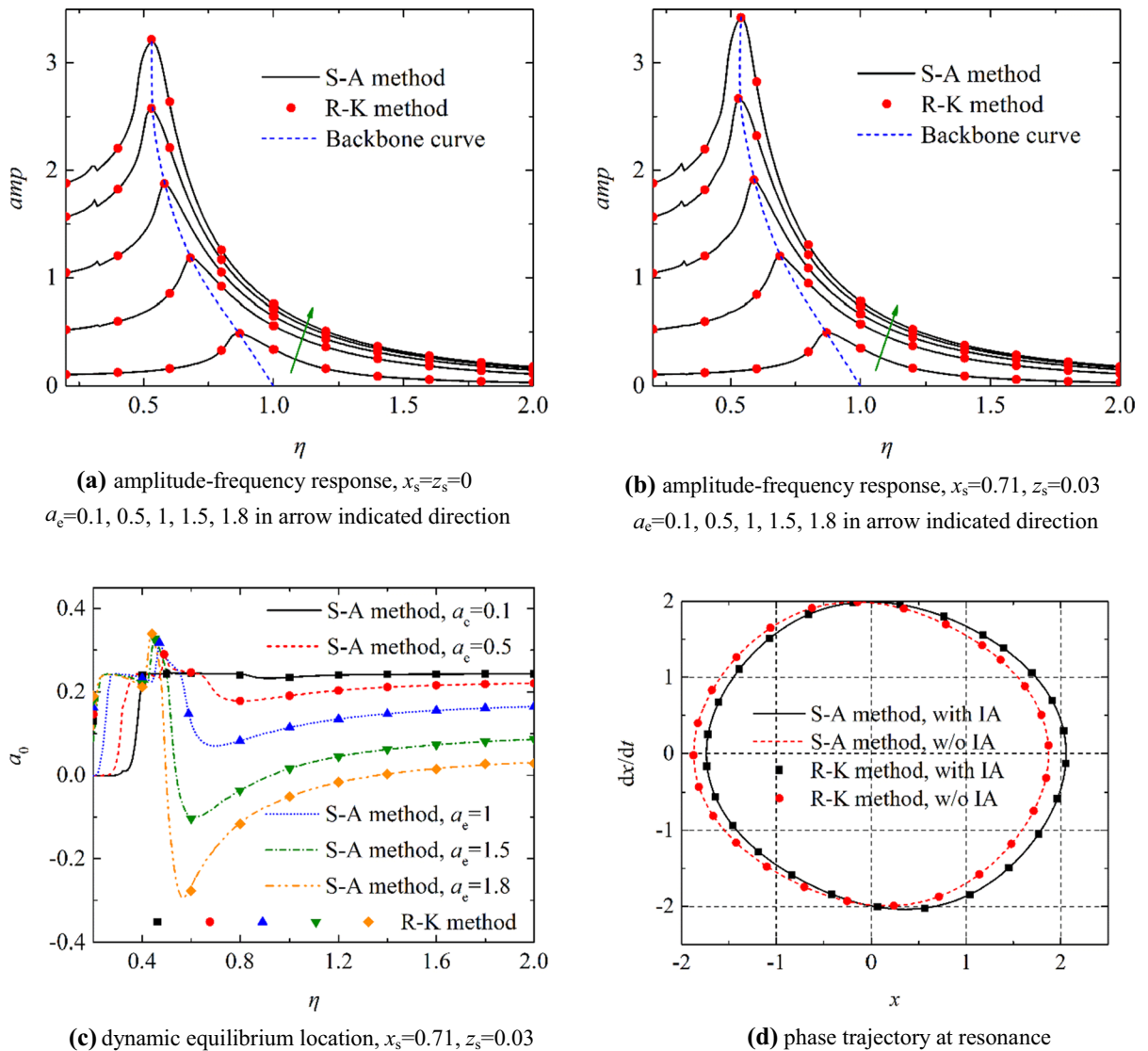


Fig. 5 Steady-state responses with different excitation amplitudes

influence on the dynamic equilibrium location than on the harmonic amplitudes.

Figure 5 shows the steady-state responses of the isolation system with different excitation amplitudes. The semianalytical results (denoted as “S–A method”) are show in lines, and the Runge–Kutta results (denoted as “R–K method”) are show in scatters. The semianalytical results coincide well with the Runge–Kutta results on all conditions shown in Fig. 5.

Amplitude–frequency responses are shown in Fig. 5a and b with the base excitation amplitudes

$a_e = 0.1, 0.5, 1, 1.5$ and 1.8 . The system is unstable when $a_e > 1.8$. The steady-state amplitude, without containing a_0 , is denoted as *amp*. The backbone curves for resonance are shown in dashed lines. With the Bouc–Wen hysteresis and the positive high-order stiffness, the system presents a softening-hardening behavior. The inertial acceleration enhances the hardening behavior and leads to higher resonant frequencies and larger resonant amplitudes. Resonant frequencies and amplitudes with (denoted as “with IA”) and without (denoted as “w/o IA”) inertial acceleration are shown in Table 1. The inertial

Table 1 Resonant frequencies and amplitudes with different excitation amplitudes

	$a_e = 0.1$	$a_e = 0.5$	$a_e = 1$	$a_e = 1.5$	$a_e = 1.8$
W/O IA					
Frequency	0.87	0.68	0.58	0.53	0.53
Amplitude	0.49	1.18	1.87	2.57	3.20
With IA					
Frequency	0.87	0.69	0.59	0.53	0.54
Amplitude	0.49	1.20	1.91	2.66	3.43

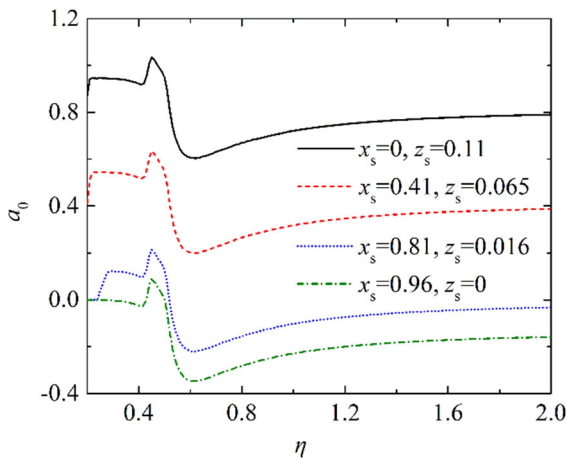


Fig. 6 Dynamic equilibrium locations with different static equilibrium states

acceleration has limited influence on the resonant frequency, and its influence on the resonant amplitude depends on the excitation amplitude.

The dynamic equilibrium locations are shown in Fig. 5c. With larger excitation amplitude, the dynamic equilibrium location changes more dramatically. Phase trajectories at resonance when $a_e = 1$ with/without the inertial acceleration are shown in Fig. 5d. It is obvious that the main difference of the two rings lies in the location rather than the shape. With inertial acceleration, phase trajectory is no longer symmetric about the origin point.

Dynamic equilibrium locations with 4 static equilibrium states are shown in Fig. 6. They all satisfy $a_{in} = 0.1$ based on Eq. (41). With larger x_s , the dynamic equilibrium location is lower. When $x_s = 0.81$ and $z_s = 0.016$, the maximum value of $|a_0|$ reaches the minimum, indicating the condition with least deviation from the static equilibrium location.

The amplitude–frequency curves are almost the same (root-mean-square difference is less than 0.1%) with 4 static equilibrium states.

5.3 Parameter analysis

This section investigates the dynamic effect of the inertial acceleration with different system parameters of k_3 , β and γ . In order to cover more conditions, parameter values in this section may exceed the parameter space which is able to be achieved by the system shown in Fig. 1. Determine the parameters as $\delta = 0.1$, $k_5 = 0$, $\beta = \gamma = 1$ and $a_e = 1$. The steady-state responses with different cubic stiffness k_3 are shown in Fig. 7. The acceleration effect on z_s changes the amplitude–frequency responses in a similar way to that on x_s , so z_s is set as 0 in Fig. 7a.

When $k_3 = 0.038$, the steady-state response is stable without inertial acceleration, while unstable with the inertial acceleration. It reveals that the inertial acceleration weakens the stability of the isolation system. With inertial acceleration, amp increases dramatically and a_0 decreases dramatically at the resonance, and jump phenomena occur. With a negative cubic stiffness, the inertial acceleration decreases the resonant frequency and the resonant amplitude. The dynamic equilibrium location reaches the maximum around the resonance and decreases gradually at higher frequencies. With a positive stiffness, the inertial acceleration has an opposite effect. A positive residual hysteretic force leads to a positive overall deviation of the dynamic equilibrium location regardless of the positive or negative high-order stiffness. Without high-order stiffness ($k_3 = 0$), the inertial acceleration has no effect on the vibration amplitude and a_0 is independent of x_s . The acceleration effect on z_s leads to a constant dynamic equilibrium deviation.

The equivalent damping ratio of the system depends on β and γ in the Bouc–Wen model. Determine the parameters as $\delta = 0.1$, $k_3 = 5 \times 10^{-3}$, $k_5 = 10^{-4}$ and $a_e = 1$. The steady-state responses with different Bouc–Wen model parameters are shown in Fig. 8. The equivalent damping ratio can be increased by increasing β/γ or $\beta + \gamma$. The higher equivalent damping ratio leads to a smaller resonant amplitude and a smaller variation of the dynamic equilibrium location. In addition, the increase of $\beta + \gamma$ enhances the stiffness-softening behavior of the Bouc–Wen

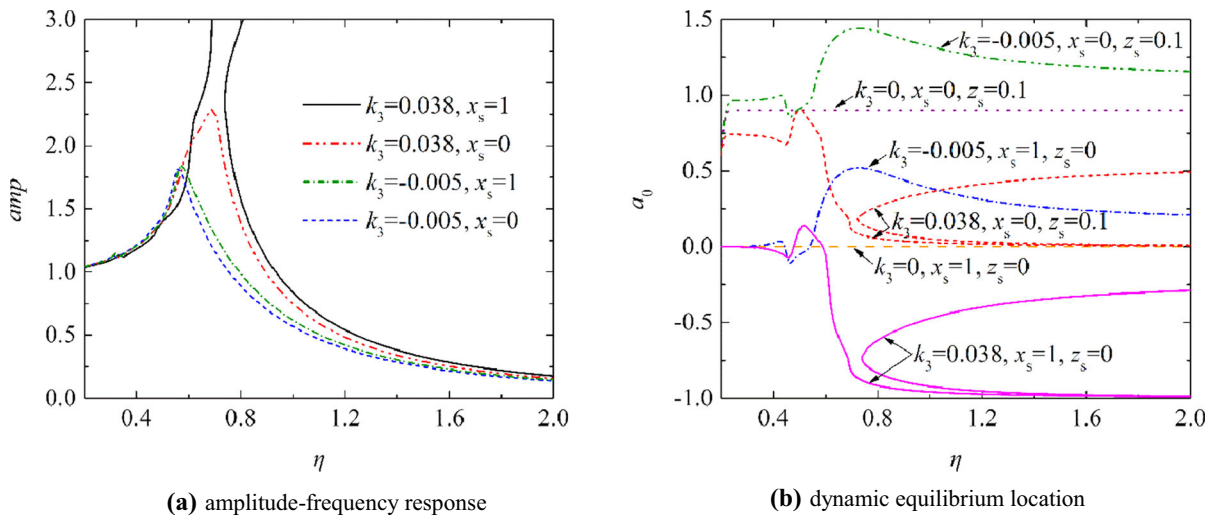


Fig. 7 Steady-state responses with different cubic stiffness

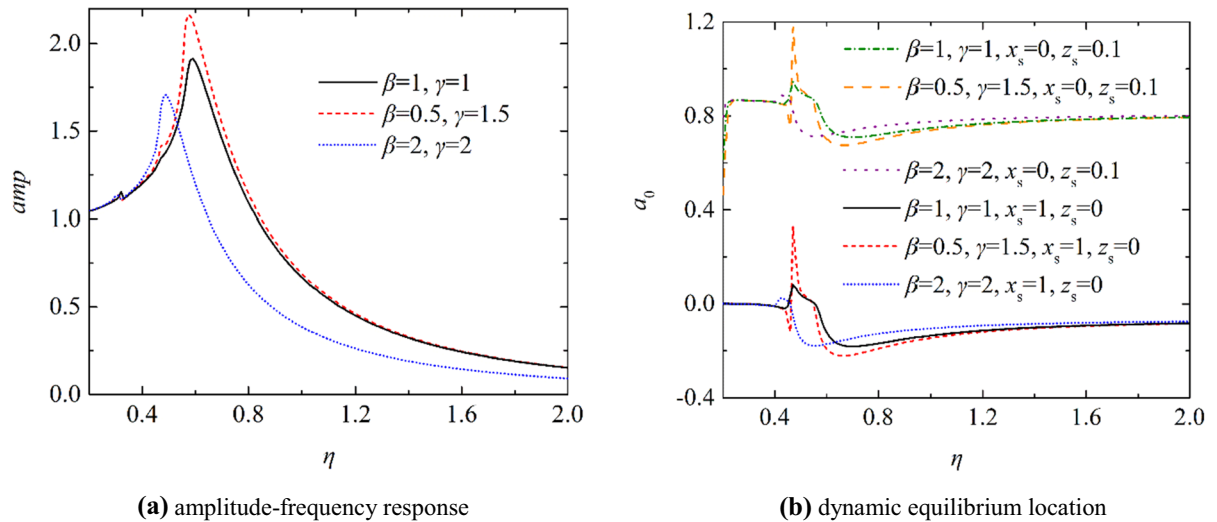


Fig. 8 Steady-state responses with different Bouc–Wen model parameters

hysteresis, and leads to the decreasing resonant frequency.

6 Conclusion

This work focuses on the dynamic effects of an inertial acceleration on a nonlinear vibration isolation system with high-order stiffness and Bouc–Wen hysteresis. A wire rope-based isolator is treated as a studied case. Analysis and simulations are performed to determine the static equilibrium states and the frequency

responses for various parameters. The key findings are summarized as follows:

1. A semianalytical method is adopted based on a harmonic balance method. The Fourier expansions of high-order terms are calculated by a proposed recursive method. The hysteresis-related terms are calculated with an alternating frequency/time domain technique. The proposed method can be used to analyze nonlinear systems containing both polynomial functions and multi-valued implicit functions. The analytical results

are verified by numerical simulations implemented by a fourth-order Runge–Kutta method.

2. An inertial acceleration affects both the static equilibrium state and the dynamic response. Due to the historical dependence of the Bouc–Wen hysteresis, an inertial acceleration may lead to diverse static equilibrium states with different paths to the equilibrium. The static equilibrium state is determined by the static equilibrium displacement and the residual hysteretic force. The inertial acceleration has separate dynamic effects on the static equilibrium displacement and the residual hysteretic force.
3. The acceleration effect on the static equilibrium displacement leads to additional coupling stiffness terms in dynamic equations and supplementary super-harmonic components in frequency responses. Specially, the effect results in even-order stiffness from higher odd-order stiffness, and thus the restoring force is no longer symmetric. With a positive high-order stiffness, the system tends to be harder with higher resonant frequency and larger resonant amplitude. The negative high-order stiffness leads to an opposite trend. Furthermore, a static equilibrium displacement has a significant influence on the dynamic equilibrium location. With a positive high-order stiffness and a positive static equilibrium displacement, the dynamic equilibrium location reaches the minimum around the resonance and increases gradually at higher frequencies.
4. The acceleration effect on the residual hysteretic force changes the amplitude–frequency responses through additional coupling stiffness in a similar way to that on the static equilibrium displacement, even though the additional stiffness is not explicitly presented in the dynamic equations. A positive residual hysteretic force leads to a positive overall deviation of the dynamic equilibrium location regardless of the positive or negative high-order stiffness.

Acknowledgements The work is supported by the National Natural Science Foundation of China [11902097, 11872159].

Compliance with ethical standards

Conflict of interest The authors declare that they have no conflict of interest.

References

1. Chen, L.Q., Li, X., Lu, Z.Q., Zhang, Y.W., Ding, H.: Dynamic effects of weights on vibration reduction by a nonlinear energy sink moving vertically. *J. Sound Vib.* **451**, 99–119 (2019)
2. Zhou, J., Xiao, Q., Xu, D., Ouyang, H., Li, Y.: A novel quasi-zero-stiffness strut and its applications in six-degree-of-freedom vibration isolation platform. *J. Sound Vib.* **394**, 59–74 (2017)
3. Zhang, Y.W., Lu, Y.N., Zhang, W., Teng, Y.Y., Yang, H.X., Yang, T.Z., Chen, L.Q.: Nonlinear energy sink with inerter. *Mechanical Systems and Signal Processing* **125**, 52–64 (2019)
4. Chen, Y.Y., Yan, L.W., Sze, K.Y., Chen, S.H.: Generalized hyperbolic perturbation method for homoclinic solutions of strongly nonlinear autonomous systems. *Applied Mathematics and Mechanics (English Edition)* **33**(9), 1137–1152 (2012)
5. Lacarbonara, W.: *Nonlinear structural mechanics*. Springer, New York (2013)
6. Yang, K., Harne, R.L., Wang, K.W., Huang, H.: Investigation of a bistable dual-stage vibration isolator under harmonic excitation. *Smart Mater. Struct.* **23**(4), 045033 (2014)
7. Wang, X.L., Zhou, J.X., Xu, D.L., Ouyang, H.J., Duan, Y.: Force transmissibility of a two-stage vibration isolation system with quasi-zero stiffness. *Nonlinear Dyn.* **87**(1), 633–646 (2017)
8. Guo, P.F., Lang, Z.Q., Peng, Z.K.: Analysis and design of the force and displacement transmissibility of nonlinear viscous damper based vibration isolation systems. *Nonlinear Dyn.* **67**(4), 2671–2687 (2012)
9. Tang, B., Brennan, M.J.: A comparison of two nonlinear damping mechanisms in a vibration isolator. *J. Sound Vib.* **332**(3), 510–520 (2013)
10. Lu, Z.Q., Brennan, M.J., Chen, L.Q.: On the transmissibilities of nonlinear vibration isolation system. *J. Sound Vib.* **375**, 28–37 (2016)
11. Yang, J., Xiong, Y.P., Xing, J.T.: Vibration power flow and force transmission behaviour of a nonlinear isolator mounted on a nonlinear base. *Int. J. Mech. Sci.* **115–116**, 238–252 (2016)
12. Huang, X.C., Sun, J.Y., Hua, H.X., Zhang, Z.Y.: The isolation performance of vibration systems with general velocity-displacement-dependent nonlinear damping under base excitation: numerical and experimental study. *Nonlinear Dyn.* **85**(2), 777–796 (2016)
13. Gao, Y.Y., Tang, G., Wan, W., Zou, S.H.: Study about nonlinear factor influence on the vibration isolation effect of damper. *Mechanics in Engineering* **37**(5), 590–596 (2015)
14. Rao, S.S.: *Mechanical Vibrations*, 5th edn. Prentice Hall, Upper Saddle River (2011)
15. Xiong, H., Kong, X.R., Li, H.Q., Yang, Z.G.: Vibration analysis of nonlinear systems with the bilinear hysteretic oscillator by using incremental harmonic balance method. *Commun. Nonlinear Sci. Numer. Simul.* **42**, 437–450 (2017)
16. Wu, R.P., Bai, H.B., Lu, C.H.: Simplified analysis of hysteresis dry friction vibration isolation system on flexible

- foundation. *Journal of Mechanical Strength* **41**(1), 44–48 (2019)
17. Sauter, D., Hagedorn, P.: On the hysteresis of wire cables in Stockbridge dampers. *Int. J. Non-Linear Mech.* **37**(8), 1453–1459 (2002)
 18. Casini, P., Vestroni, F.: Nonlinear resonances of hysteretic oscillators. *Acta Mech.* **229**(2), 939–952 (2018)
 19. Wong C W, Ni Y Q, Lau S L. Steady-state oscillation of hysteretic differential model. I: response analysis. *Journal of Engineering Mechanics*. 1994, 120(11): 2271–2298.
 20. Lacarbonara, W., Vestroni, F.: Nonclassical responses of oscillators with hysteresis. *Nonlinear Dyn.* **32**(3), 235–258 (2003)
 21. Yuan, T.C., Yang, J., Chen, L.Q.: A harmonic balance approach with alternating frequency/time domain progress for piezoelectric mechanical systems. *Mechanical Systems and Signal Processing* **120**, 274–289 (2019)
 22. Zhang, Z., Chen, Y.: Harmonic balance method with alternating frequency/time domain technique for nonlinear dynamic system with fractional exponential. *Applied Mathematics and Mechanics (English Edition)* **35**(4), 423–436 (2014)
 23. Foti F, Martinelli L. Hysteretic behavior of Stockbridge dampers: modelling and parameter identification. *Mathematical Problems in Engineering*, 2018: 8925121.
 24. Balaji, P.S., Rahman, M.E., Moussa, L., Lau, H.H.: Wire rope isolators for vibration isolation of equipment and structures -a review. *IOP Conference Series: Materials Science and Engineering* **78**(18), 012001 (2015)
 25. Carpineto, N., Lacarbonara, W., Vestroni, F.: Hysteretic tuned mass dampers for structural vibration mitigation. *J. Sound Vib.* **333**(5), 1302–1318 (2014)
 26. Carboni, B., Lacarbonara, W.: Nonlinear dynamic characterization of a new hysteretic device: experiments and computations. *Nonlinear Dyn.* **83**(1), 23–39 (2016)
 27. Carboni, B., Lacarbonara, W., Brewick, P., Masri, S.: Dynamical response identification of a class of nonlinear hysteretic systems. *J. Intell. Mater. Syst. Struct.* **29**(13), 2795–2810 (2018)
 28. Carboni, B., Lacarbonara, W.: Nonlinear vibration absorber with pinched hysteresis: theory and experiments. *Journal of Engineering Mechanics* **142**(5), 04016023 (2016)
 29. Awtar, S., Sen, S.: A generalized constraint model for two-dimensional beam flexures: nonlinear load-displacement formulation. *J. Mech. Des.* **132**, 081008 (2010)
 30. Carboni, B., Lacarbonara, W., Auricchio, F.: Hysteresis of multiconfiguration assemblies of Nitinol and steel strands: experiments and phenomenological identification. *Journal of Engineering Mechanics* **141**(3), 04014135 (2015)

Publisher's Note Springer Nature remains neutral with regard to jurisdictional claims in published maps and institutional affiliations.